Two-level simulation of injection-induced fracture slip and wing-crack propagation in poroelastic media

Hau Trung Dang [*], Inga Berre, Eirik Keilegavlen

Center for Modeling of Coupled Subsurface Dynamics, Department of Mathematics, University of Bergen, Norway

A B S T R A C T

In fractured poroelastic media under high differential stress, the shearing of pre-existing fractures and faults and propagation of wing cracks can be induced by fluid injection. This paper presents a two-dimensional mathematical model and a numerical solution approach for coupling fluid flow with fracture shearing and propagation under hydraulic stimulation by fluid injection. Numerical challenges are related to the strong coupling between hydraulic and mechanical processes, the material discontinuity the fractures represent in the medium, and the strong effect that fracture deformation and propagation have on the physical processes. The solution approach is based on a two-level strategy that is classified into the coarse and fine levels. In the coarse level, flow in and poroelastic deformation of the matrix are coupled with the flow in the fractures and fracture contact mechanics, allowing fractures to frictionally slide. Fracture propagation is handled at the fine level, where the maximum tangential stress criterion triggers the propagation of fractures, and Paris' law governs the fracture growth processes. Simulations show how the shearing of a fracture due to fluid injection is linked to fracture propagation, including cases with hydraulically and mechanically interacting fractures.

1. Introduction

In the hydraulic stimulation of geothermal reservoirs in igneous rocks, elevated pressures in combination with anisotropic stress conditions result in shear displacement and the dilation of fractures and faults favorably oriented to slip, propagation of wing cracks from sliding or shearing fractures, and/or propagation of hydraulic fractures.[1–4] Sliding, dilation, and the propagation of fractures affect the stress and flow regime in the formation and, thereby, the stress state and deformation of nearby fractures. The coupling between flow in fractured and faulted rocks, fracture slip and propagation, and poromechanical matrix deformation is strong: fracture propagation occurs locally but impacts and interacts with macroscopic reservoir-scale flow and deformation of the fractured rock.

The current work presents a modeling approach for hydraulic stimulation of fractured reservoirs under anisotropic stress. In this case, depending on the elevation of fluid pressure, the stimulation will cause slip of pre-existing fractures as well as fracture propagation. Slips of pre-existing fractures occur when coupled hydromechanical processes induced by fluid injection result in changes to the effective stress regime so that the fracture's frictional resistance to slip is exceeded.[5,6] The

stress alterations resulting from fracture slip are coupled with fluid pressurization and drive tensile propagation of wing cracks at the fracture's tips. Hence, in contrast to most of the research literature on fracture propagation resulting from hydraulic stimulation, this work does not only consider the development of tensile hydrofractures. Instead, the reservoir stimulation is caused by a combination of slip of pre-existing fractures with fracture propagation.[1–3] Following McClure and Horne,[2] we refer to this as mixed-mechanism stimulation.

To fully represent how injection operations alter fractured rock characteristics, simulation models must capture both the slip and deformation of existing fractures as well as fracture propagation. In addition, they must be able to account for the heterogeneous characteristics of subsurface formations. Challenges are related to capturing how the hydromechanical processes in the matrix interact with the flow, deformation, and propagation of fractures. This includes accounting for fracture contact mechanics, with the possibility of fractures being closed, sliding, and open.

To model the physics of these phenomena, fractures must be represented explicitly in an otherwise intact porous medium, conceptually leading to a discrete fracture-matrix model. To avoid resolving thin fractures in their normal direction, fractures are represented as co-
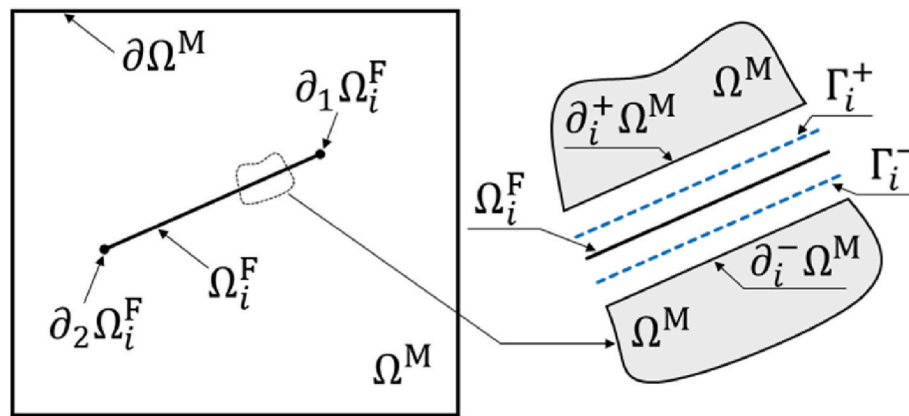
Fig. 1. Illustration of a fracture, Ω_i^F and a host medium, Ω^M.

dimension one objects embedded in the host medium with corresponding dimensionally reduced equations, resulting in a mixed-dimensional model.[7] Discretizations of such models can be both nonconforming and conforming. While conforming methods align the computational grid to the fractures, nonconforming methods utilize enrichment functions to capture the effects of the fractures. Recently, the nonconforming XFEM methodology, which has previously been developed for hydraulic fracture propagation,[8–11] has been extended to couple fracture propagation with fracture contact mechanics in impermeable media.[12,13] A conforming method allows the direct assignment of variables and governing equations to the host medium, the fracture, and the matrix-fracture interface. For fluid flow, this flexibility simplifies the task of correctly capturing fluid exchange within and between fractures and the matrix. Furthermore, a conforming fracture representation allows for the modeling of fracture contact mechanics in poroelastic media,[9,10,14–16] including fracture propagation[17,18] in a manner that directly couples shear and normal displacements along the fracture with alterations in stress and flow regime.[19]

In numerical modeling of fracture mechanics in porous media caused by fluid injection, numerical models have generally focused either (1) on the tensile propagation of hydraulic fractures or (2) the deformation of pre-existing fractures or faults. The first regime ignores the deformation of existing fractures caused by frictional contact and governs the growth of fractures by Mode I fracturing.[8,10,15,20–31] The second regime focuses on the frictional sliding, dilation and/or opening of pre-existing fractures or faults without considering fracture propagation.[11,19,32–37] Some recent models couple both regimes.[2,18,19,38] However, the coupling of hydromechanical processes between fractures and the matrix and the fracture propagation in these models are typically based on strong assumptions. For example, fracture dilation is assumed to not affect the surrounding stress[2,18] and restrictions allow fractures to propagate only along predefined paths[2] or the edges of fixed grid cells.[18,38–41]

This work presents a numerical model, based on conforming discretizations, for injection-induced fracture shear-deformation and wing-crack propagation in poroelastic media without these limitations. Biot's model for poroelasticity governs flow and deformation in the matrix, with the deformation of fractures represented by contact mechanics, which consider the fractures' frictional resistance to sliding.[19] The fracture growth process is governed by the maximum tangential stress criterion and Paris's law.[42,43] A primary motivation for our work is to enable simulations on domains that are too large for the fracture propagation to be resolved in detail. To that end, we separate the poroelastic matrix deformation and fracture shearing from the fracture propagation in a two-level approach. A relatively coarse grid can be accepted for flow, poroelastic matrix deformation, and fracture deformation. In contrast, to capture the stress and correctly evaluate fracture propagation, a refined grid is needed around the fracture tip. As fracture propagation occurs locally from the fracture's tips,[2,44] an efficient solution

strategy can be defined based on multilevel methods,[45–47] which in this work is cast in the language of the heterogeneous multiscale approach.[45,48] Flow, poroelastic deformation, and contact mechanics of fractures are evaluated in a coarse-level model, and mechanical fracture propagation is evaluated in a local fine-level model[48] subject to body forces and boundary conditions that also account for the influence of macroscale fluid pressure. The models are coupled via displacement fields close to fracture tips (coarse level to fine level) and updates to the fracture path (fine level to coarse level).

In discretizing the coarse-level model, a finite volume method for fracture and matrix flow and poroelastic matrix deformation is combined with an active set strategy for fracture contact mechanics.[19] For fracture propagation on the fine level, a finite element method is applied in combination with collapsed quarter-point elements at the fracture tips to capture their stress singularity.[17,49] Adaptive remeshing is introduced on both levels to account for fracture propagation based on the implementation by Dang-Trung et al.[17] This work presents numerical examples that focus on the method's ability to balance accuracy and computational cost under variations in grid resolution and the parameters which govern the coupling between the coarse- and fine-level modeling. This work also presents a case with multiple hydromechanically coupled fractures, showcasing the capacity of our methodology to solve complex problems.

The paper is structured as follows. Section 2 presents the governing equations and Section 3 presents the two-level solution strategy. Section 4 presents a numerical approach that employs a novel combination of a finite volume method for the poroelastic deformation of existing fractures with a finite element approach for the fracture propagation process. Section 5 presents several numerical test cases to show the stability and accuracy of the proposed approach and its potential in settings where multiple fractures mutually affect each other.

2. Mathematical model

The mathematical model for injection-induced fracture shear deformation and wing-crack propagation in poroelastic media is based on systems of partial differential equations and KKT conditions governing the physics. We start by introducing notations of geometry and primary variables. Then, we present the mathematical model for fracture contact mechanics, poroelastic deformation of the matrix, and fluid flow. At the end of this section, we present the model for the fracture propagation process.

2.1. Geometry and primary variables

As shown in Fig. 1, we represent a fractured porous media as a two-dimensional domain Ω that is divided into a host medium, termed the matrix and denoted Ω^M, and a set of fractures that are considered to be

one-dimensional objects embedded in Ω^{M}. From here on, we will refer to both fractures and faults simply as fractures and let Ω_i^{F} denote fracture i and $\partial_k \Omega_i^{\mathrm{F}}, k = \{1, 2\}$ represent the two tips of Ω_i^{F}. Throughout the paper, we assume that fractures do not intersect. Finally, we denote the interface between Ω^{M} and Ω_i^{F} by Γ_i, where, when needed, we shall represent the two sides of the interface by Γ_i^+ and Γ_i^-. The boundary of Ω^{M} that coincides with $\Gamma_i^{\pm}$ is denoted $\partial_i^{\pm} \Omega^{\mathrm{M}}$.

The primary variables are displacements, fluid pressures, contact forces on the fractures, and fluid fluxes between fractures and the matrix. Specifically, the displacements on Ω^{M} are denoted as $\mathbf{u}$, the pressure is represented by p in Ω^{M} and p_i in Ω_i^{F}, and the contact force $\mathbf{f}_i$ is defined only in Ω_i^{F}. Finally, $\mathbf{u}_i^{\pm}$ and $\lambda_i^{\pm}$ denote the displacement and fluid flux on $\Gamma_i^{\pm}$, respectively. Time derivatives are denoted by a dot, e.g., $\dot{\mathbf{u}}_i$.

2.2. Fracture contact mechanics

Let $\mathbf{n}_i$ be the normal vector to the fracture surface Ω_i^{F}, pointing from Γ_i^+ to Γ_i^-. We define the jump operator acting on $\mathbf{u}_i$ by

$$[\![\mathbf{u}_i]\!] = ([\![\mathbf{u}_i]\!]_{\mathrm{n}}, [\![\mathbf{u}_i]\!]_{\tau}) = \mathbf{u}_i^- - \mathbf{u}_i^+, \tag{1}$$

where $[\![\mathbf{u}_i]\!]_{\mathrm{n}}$ and $[\![\mathbf{u}_i]\!]_{\tau}$ denote the normal and tangential components of the displacement jump, respectively. In the normal direction, we require nonpenetration and define the normal component of the contact traction, $\mathbf{f}_{i,\mathrm{n}}$, to be negative in contact. This assumption gives rise to the KKT condition, i.e.

$$[\![\mathbf{u}_i]\!]_{\mathrm{n}} - g \geq 0, \mathbf{f}_{i,\mathrm{n}} \leq 0, ([\![\mathbf{u}_i]\!]_{\mathrm{n}} - g)\mathbf{f}_{i,\mathrm{n}} = 0. \tag{2}$$

Here, the gap function g allows the fracture to open while the walls are still in mechanical contact. We set $g = [\![\mathbf{u}_i]\!]_{\tau} \tan \psi$, with ψ being the dilation angle to let the fracture open due to tangential slip.

The tangential motion of the fracture is modeled as a frictional contact problem, with the following relation between the tangential contact traction, $\mathbf{f}_{i,\tau}$, and the change of displacement jump in time, $[\![\dot{\mathbf{u}}_i]\!]_{\tau}$:

$$\begin{aligned} |\mathbf{f}_{i,\tau}| &\leq -\mu_s \mathbf{f}_{i,\mathrm{n}}, \\ |\mathbf{f}_{i,\tau}| &< -\mu_s \mathbf{f}_{i,\mathrm{n}} \quad \text{so} \quad [\![\dot{\mathbf{u}}_i]\!]_{\tau} = 0, \\ |\mathbf{f}_{i,\tau}| &= -\mu_s \mathbf{f}_{i,\mathrm{n}} \quad \text{so} \exists \gamma \in \mathbb{R}, \mathbf{f}_{i,\tau} = -\gamma^2 [\![\dot{\mathbf{u}}_i]\!]_{\tau}. \end{aligned} \tag{3}$$

The tangential traction is bounded from above by the normal traction scaled by the friction μ_s, and when the frictional resistance is overcome, the displacement is parallel to the tangential traction.

The force balance on the fracture's surfaces is given by

$$\mathbf{n}_i \cdot \boldsymbol{\sigma}|_{\partial_i^+ \Omega^M} = \mathbf{f}_i - \alpha_i p_i(\mathbf{I} \cdot \mathbf{n}_i), -\mathbf{n}_i \cdot \boldsymbol{\sigma}|_{\partial_i^- \Omega^M} = \mathbf{f}_i - \alpha_i p_i(\mathbf{I} \cdot \mathbf{n}_i), \tag{4}$$

where $\boldsymbol{\sigma}$ denotes the hydromechanical stress in the matrix, $\mathbf{f}_i$ is the contact traction acting on the fracture surface, and p_i is the pressure inside the fracture. The Biot coefficient in the fracture is denoted by α_i and $\mathbf{I}$ is the identity matrix. Equality should be enforced on $\Gamma_i^{\pm}$, but for notational convenience, we have suppressed projection operators. See Keilegavlen et al.[50] for more information.

2.3. Flow and poroelastic deformation of matrix

Flow and deformation in Ω^{M} are modeled by Biot theory, with the matrix taken as a linearly elastic medium. By neglecting inertial terms, the conservation of momentum and mass is governed by

$$\nabla \cdot \boldsymbol{\sigma} = \mathbf{b}, \tag{5}$$

$$\alpha \frac{\partial (\nabla \cdot \mathbf{u})}{\partial t} + M \frac{\partial p}{\partial t} - \nabla \cdot \left(\frac{\mathscr{K}}{\mu} \nabla p \right) = q, \tag{6}$$

where $\boldsymbol{\sigma}$ is the hydromechanical stress in Ω^{M}, defined by

$$\boldsymbol{\sigma} = \mathbf{C} \nabla_s \mathbf{u} - \alpha p \mathbf{I}. \tag{7}$$

Here, ∇_s represents the symmetrized gradient, $\mathbf{C}$ is the stiffness matrix, $\mathbf{b}$ denotes body forces, and q is the fluid source term. The Biot coefficient of the matrix is α, the Biot modulus is given by $M = \left(\varphi c_p + \frac{\alpha - \varphi}{K} \right)$, c_p is the fluid compressibility, φ is the matrix porosity, K is the bulk modulus, $\mathscr{K}$ denotes the permeability of the porous matrix, which is assumed to be isotropic, and μ is the fluid viscosity. On $\partial_i^{\pm} \Omega^{\mathrm{M}}$, continuity of the displacements is enforced so that $\mathrm{tr}\, \mathbf{u}|_{\partial_i^{\pm} \Omega^M} = \mathbf{u}_i^{\pm}$, where tr is the trace operator. As seen from Ω^{M}, the interface displacement thus acts as a Dirichlet boundary condition. The interface fluid flux λ_i enters as a Neumann condition to the mass conservation equation.

2.4. Fluid flow in fractures and matrix-fracture interaction

By using the discrete fracture-matrix model, the fracture is represented explicitly in the domain. Following Stefansson et al.,[19] who extended the work of Martin et al.[51] to discrete fracture-matrix models with changing apertures, the conservation of mass in fracture i is given by

$$\frac{\partial a_i}{\partial t} + a_i c_p \frac{\partial p_i}{\partial t} - \nabla \cdot \left(\frac{\mathscr{K}_i}{\mu} \nabla p_i \right) + (\lambda_i^+ + \lambda_i^-) = q_i. \tag{8}$$

Here, we assume that the fracture can be completely occupied by the fluid, i.e., that the fracture porosity and Biot's coefficient are equal to one. $\mathscr{K}_i$ is the fracture tangential transmissivity. The aperture $a_i = a_i^0 + [\![\mathbf{u}_i]\!]_{\mathrm{n}}$ is computed by a sum of an initial value a_i^0 and an update due to fracture deformation. Therefore, the first term in Eq. (8) represents volume changes due to changes in aperture. The fracture transmissivity is related to aperture by the so-called cubic law, $\mathscr{K}_i = a_i^3/12$ [52]; i.e., a_i equals the hydraulic aperture of the fracture. The term $(\lambda_i^+ + \lambda_i^-)$ represents inflow from the matrix over $\Gamma_i^{\pm}$, where $\lambda_i^{\pm}$ is the interface flux between the matrix and the fracture defined as

$$\lambda_i^{\pm} = -\kappa_i(p_i - \mathrm{tr}\, p^{\pm}), \tag{9}$$

where $\kappa_i = 2\mathscr{K}_i/(\mu a_i^2)$ is an expression of permeability normal to the fracture, $p^{\pm}$ represents pressures from the matrix at the two sides of the fracture, and it is understood that the fracture and matrix pressures should be projected onto $\Gamma_i^{\pm}$.

2.5. Fracture propagation

The propagation criterion is based on a criterion on maximum tangential stress[42] for mixed-mode fracturing. The theory postulates propagation when the maximum tangential stress in the process zone around a fracture tip exceeds a critical value. The direction of propagation is that of the maximum tangential stress. The tangential stress around a fracture tip can be expressed in polar coordinates as

$$\sigma_{\theta}^{\mathrm{L}}(r, \theta) = \frac{1}{\sqrt{2\pi r}} \left(K_{\mathrm{I}} \cos^3 \frac{\theta}{2} - \frac{3}{2} K_{\mathrm{II}} \cos \frac{\theta}{2} \sin \theta \right) \tag{10}$$

and the crack grows in the direction θ_0 if $\sigma_{\theta}^{\mathrm{L}}(r, \theta_0) = \frac{K_{\mathrm{IC}}}{\sqrt{2\pi r}}$, where K_{IC} is the fracture toughness. The propagation angle is given by

$$\theta_0 = 2 \tan^{-1} \left(\frac{K_{\mathrm{I}}}{4K_{\mathrm{II}}} \pm \frac{1}{4} \sqrt{\left(\frac{K_{\mathrm{I}}}{K_{\mathrm{II}}} \right)^2 + 8} \right) \tag{11}$$

subjected to a condition

$$K_{\mathrm{II}} \left(\sin \frac{\theta_0}{2} + 9 \sin \frac{3\theta_0}{2} \right) < K_{\mathrm{I}} \left(\cos \frac{\theta_0}{2} + 3 \cos \frac{3\theta_0}{2} \right) \tag{12}$$

where r is the distance from the tip. K_{I} and K_{II} are the stress intensity
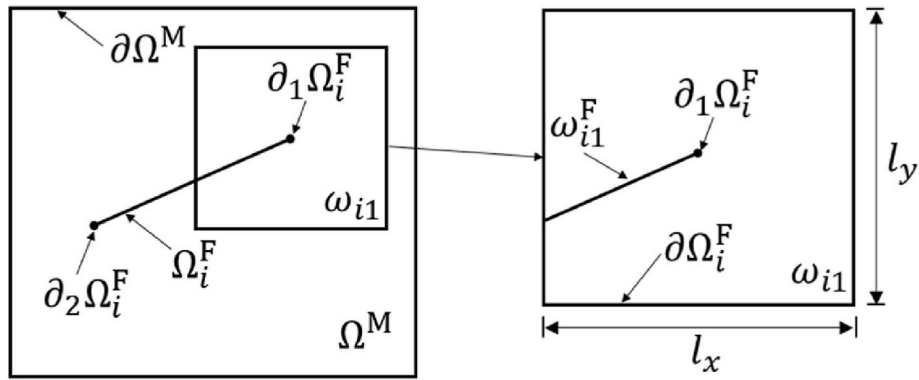
Fig. 2. Illustration of a fracture, Ω_i^F and a fine-level domain ω_{ik}.

factors (SIFs). The propagation length can, in general, be computed by a Paris-type law,[43] which, under the assumption that there is a single fracture inside every fine-level domain, simplifies to a propagation length equal to a preset value, $l_{\max}$. If more than one crack grows simultaneously, then the tips with the higher energy in the fracture set advance further than the others. The increment for each tip is defined by

$$l_{adv}^i = l_{\max} \left(\frac{G_i}{\max(G_i)} \right)^{0.35} \tag{13}$$

where G_i is the energy release rate for the ith propagation crack.[53]

3. Two-level solution strategy

Our goal is to define a computational approach for the interaction between, on the one hand, deformation of fractures and domains due to hydromechanical stresses and, on the other hand, the propagation of fractures. While a fully coupled approach to the governing equations presented in the previous section is possible, it is impractical for three reasons. First, compared to the time scale of fluid flow, wing-crack propagation can be considered quasi-static and can therefore be loosely coupled to the fluid flow problem.[20,54] Second, there will be no wing-crack propagation for significant periods, and efficiency can be gained by considering only the coarse-level problem. Third, while it is critical for the propagation problem to accurately capture the stress in the vicinity of the propagating fracture, including the singularity at the tip, the mechanical response of the more expansive reservoir, including other (potentially propagating) fractures, can be given a coarser representation.

Motivated by these observations, our computational model is based on a two-level approach. We define subproblems for, on the one hand, large-scale fluid flow and deformation of fractures and the matrix, and on the other hand, fracture propagation and accompanying deformation locally around fracture tips. Reflecting the small time and length scales involved in propagation, we assign separate, small domains around each fracture tip to be used in the purely mechanical propagation calculation, referred to as the fine-level problem. Conversely, the whole simulation domain is referred to as the coarse-level domain, on which we solve the problem consisting of fluid flow and fracture and matrix deformation.

3.1. Coarse- and fine-level models

The coarse-level problem is defined on the geometry presented in Section 2, with the governing equations given by Eqs. (1)–(9), that is, frictional contact mechanics coupled with hydromechanical deformation in the matrix and on the fracture domains. Fracture propagation is not explicitly accounted for in the coarse-level model but is instead updated from the solution to the fine-level problem, as discussed in Section 3.2.

As shown in Fig. 2, the fine-level models are centered on fracture tips. With each fracture tip $\partial_k \Omega_i^F$ in the coarse-level domain, we associate a (generally) smaller domain, termed a fine-level domain, and denoted as ω_{ik} with size $l_x \times l_y$. The fine-level domain is composed of a part of the matrix, $\omega_{ik} \subset \Omega^M$, and a single fracture domain, ω_{ik}^F, which represents a part of the fracture Ω_i^F in the coarse-level domain. In general, $\omega_{ik}^F \not\subset \Omega_i^F$ since the resolution of the propagating fracture is different in the fine-level and coarse-level domains that will be discussed in Section 4. We let $\partial_i^{\pm} \omega_{ik}$ represent the two sides of the fine-level fracture while $\partial_M \omega$ is the rest of the boundary of ω_{ik}.

In accordance with the discussion at the beginning of this section, we include the effect of fluid pressure as a body force in the fine-level model. The primary variable in the fine-level problem is, therefore, the displacement in ω_{ik}, which we represent by $\mathbf{u}^L$ for simplicity. As with the full deformation, we assume that the fine-level matrix behaves similarly to a linearly elastic and isotropic medium governed by

$$\nabla \cdot \mathbf{c} \nabla_s \mathbf{u}^L = \mathbf{b} \tag{14}$$

where $\mathbf{b} = \nabla \cdot (\alpha p \mathbf{I})$ is the body force caused by pressure in the coarse-level domain. $\mathbf{c}$ is the stiffness tensor. Boundary conditions for the fine-level problem are set according to the coarse-level state, as discussed next.

3.2. Coupling between coarse-level and fine-level models

For the fine-level problem, the fracture surfaces are not allowed to move freely. Instead, their displacement is set from the coarse-level behavior close to the fracture tip. That is, the fine-level boundary condition on $\partial_i^{\pm} \omega_{ik}$ is given as a displacement jump computed from the coarse-level state,

$$[\![\mathbf{u}^L]\!]\big|_{\partial_i^{\pm} \omega_{ik}} = \mathscr{R}\left([\![\mathbf{u}_i]\!]\big|_{\partial_i^{\pm} \Omega^M} \right), \tag{15}$$

where $\mathscr{R}$ is a reconstruction operator, defined for the discrete problem in Section 4.4. On the remainder of the boundary, $\partial \omega_{ik}$, we similarly set

$$\mathbf{u}^L\big|_{\partial \omega_{ik}} = \mathscr{R}(\mathbf{u}). \tag{16}$$

The coupling from the fine-level model to coarse-level model consists of updating the coarse-level fracture geometry based on fine-level fracture propagation. This is linked to the continuous representation of the evolving geometry in the two models. For simplicity, we will represent the fractures as piecewise linear objects with a resolution related to that of the computational grids on the two scales, as detailed in Section 4. However, to cover more advanced features, including merging of fractures and three-dimensional problems, more elaborate geometric representations are needed.[55,56]

4. Numerical approach

This section describes the building blocks of our numerical approach in terms of grids and solution approaches to coarse-level and fine-level problems, together with the two-level coupling concept.

4.1. Numerical grids for fracture propagation

We construct numerical grids to conform to fractures in both the coarse-level and fine-level domains. That is, the grids on both Ω^{M} and ω_{ik} are constructed so that fractures coincide with the paths of grid faces and then split nodes and faces along these paths, as done by Dang-Trung et al.[17] In the coarse-level domain, we further construct one-dimensional grids on Ω_i^{F}, as well as on the interfaces $\Gamma_i^{\pm}$.

Focusing on a single fine-level domain, we represent the mesh size in a fine-level grid by Δh and let ΔH represent the coarse-level mesh size around the same fracture tip. To ensure the stability of the propagation, the resolution of the fine-level domain is set to be finer than that of the coarse-level domain, i.e., $\Delta h = \varepsilon_{\mathrm{m}} \Delta H$ with $\varepsilon_{\mathrm{m}} \leq 1$. On both scales, we consider simplex grids, with the initial grids being constructed by Gmsh.[57] Updates to the fracture geometry will generally not follow existing paths of grid faces at both the fine level and coarse level. Thus, before fracture propagation on either the fine-level domain or coarse-level domain, the grid is adjusted in the vicinity region of radius $5 \times l_{\max}$ around the fracture tip with triangular rosette elements, size Δh or ΔH, to accommodate the extension of the fracture, followed by Laplacian smoothing to preserve the grid quality.[17] This technique is effective in removing degenerate and small elements. The fracture is then prolonged by splitting grid faces and nodes. For the coarse-level grid, it is further necessary to prolong the grid for the fracture domain Ω_i^{F} and the interfaces $\Gamma_i^{\pm}$ and to update the projections between the different grids.

We remark that although the grid adjustment necessitates an update of the discretization in Ω^{M}, the cost of this operation can be limited by confining the adjustment to a region close to the fracture tip.

4.2. Coarse-level discretization

The governing equations (1)–(9) on the coarse level, namely poroelastic deformation in Ω^{M} and both fluid flow and contact mechanics in Ω_i^{F} and over Γ_i are discretized and solved fully coupled by the open-source software tool PorePy.[50] The overall approach has been used before to study poroelastic[32,33] and thermoporoelastic[19] deformation coupled with fracture mechanics and has also been applied to field studies.[58]

The discretization of the frictional contact problem requires handling the discontinuity in the contact conditions Eqs. (2)–(4). These are evaluated cellwise to determine whether fractures are open or closed and, if closed, whether they are sticking or slipping; see Stefansson et al.[19] for details. This classification is employed in an active set method, where the contact conditions and balance of forces expressed are discretized according to the state from the previous iteration.[19,33,59]

The conservation equations for flow in Ω^{M} and Ω_i^{F} as well as momentum in Ω^{M} are discretized by a family of cell-centered multipoint finite volume methods developed for poroelasticity.[60,61] The methods are based on constructing discrete representations of stresses (respective fluxes) over cell faces regarding displacements (respectively pressures) in nearby cell centers. The balance of momentum and mass is enforced on the cells. For fracture domains, the method reduces to the well-known two-point flux method, which can also deal with nonplanar domains resulting from fracture propagation. Finally, the coupling between the matrix and fractures follows the scheme described by Nordbotten et al.[14] for the flow problem.

The coupled set of equations is nonlinear and requests an iteration solver due to the active set approach to the contact conditions. The
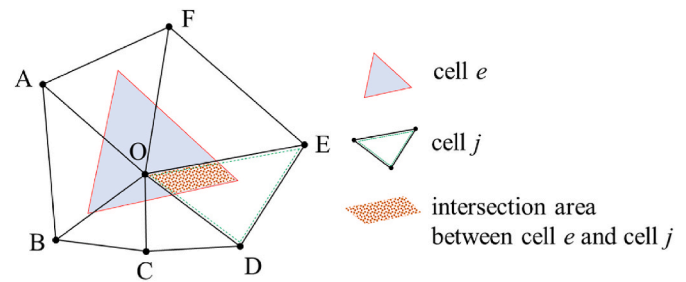

Fig. 3. Interpolation of coarse-level variables after an update of the coarse-level grid. The variables in cell e in the new grid is reconstructed from the old grid, with cells O-ABCDEF, using a nearest neighbor interpolation. The intersection area determines the weight of cell ODE to the variables for the cell e.

system is solved by a semismooth Newton method using a direct solver for the linearized system.

4.3. Fine-level discretization

While our coarse-level discretization was chosen to comply with conservation, calculations meant to decide whether a fracture will propagate, and if so, where it will go, pose different requirements on the spatial discretizations. Specifically, it is crucial to represent the stress singularity at the fracture tip. To that end, Eq. (14) is discretized by a finite element method with $\mathscr{P}_2$ basis functions. The stress singularity is captured using the nodal displacement correlation technique[62] based on quarter-point elements.[49] To enhance computational accuracy, the fine-level grid is refined and guided by residual-based a posteriori error estimates.[63] From a computed displacement field, SIFs are estimated to determine whether the fracture should propagate and, if so, in which direction.[17,62] The fine-level grid is updated as described in Section 4.1, and the displacement and pressure variables are mapped to the new grid by a $\mathscr{P}_1$ interpolation. For details of the algorithm and investigations of its performance on SIFs convergence and fracture propagation verification, we refer to Dang-Trung et al.[17]

Depending on the boundary conditions, several propagation steps may be needed to arrive at a stable state. During these iterations, the boundary conditions are fixed, consistent with the assumption that fine-level propagation is instantaneous relative to dynamics on the coarse level.

4.4. Discrete mapping between coarse-level and fine-level models

4.4.1. Mapping of variables

To couple the numerical states on the coarse-level and fine-level domains, it is necessary to project displacements from the coarse-level to fine-level domain boundaries and compress fine-level updates to the fracture geometry onto the coarse-level grid. It should be noted that, the solutions are naturally determined at the cell centers in the coarse-level grid and the nodes in the fine-level grid. Therefore, we use three processes named cell center to cell center (C2C), node to node (N2N), and cell center to node (C2N) for the mapping.

The C2C projects variables between cells in the coarse-level grid. If a fracture propagates in the coarse-level domain, the corresponding grid is locally adjusted to ensure the fracture path coincides with faces and, therefore, the variables at cell centers on the adjusted grid also need to be reconstructed. We use the natural neighbor interpolation as illustrated in Fig. 3 for this projection. We assume that new cell e interacts with old cells O-ABCDEF. The variables at the center of cell e will be reconstructed by the variables at the centers of cells O-ABCDEF, such that.
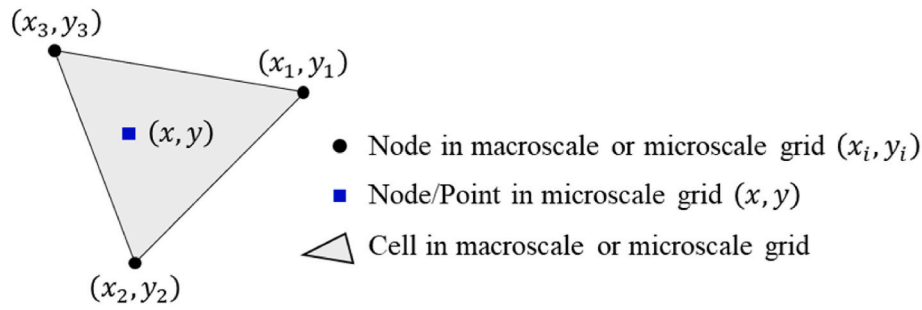
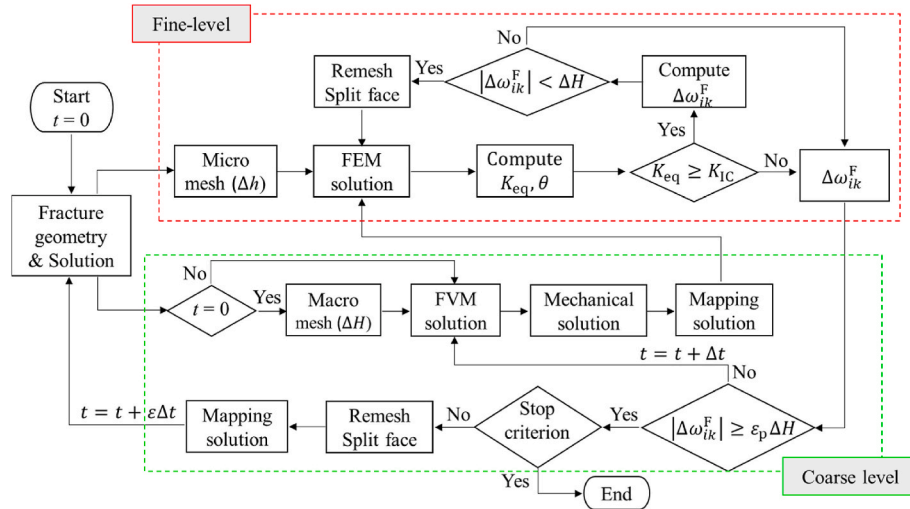**Fig. 4.** The $\mathscr{P}_1$ interpolation.

Fig. 5. Illustration of the workflow in the two-level simulation method. The simulation is controlled by the coarse-level grid size ΔH, time step size Δt, fine-level domain size l, relation between fine-level grid and coarse-level grid size ε_m and coarse-level resolution of the fracture ε_p. The details of the "Remesh/Split face" box are given in Section 4.1.

$$\xi_e = \frac{1}{\sum\limits_{j=1}^{n} A_{ej}} \sum_{j=1}^{n} A_{ej}\xi_j, \qquad (17)$$

where ξ_j denotes variables at the center of cell j, and A_{ej} is the intersection area.

The N2N projects variables from the coarse-level grid to the fine-level grid or between the fine-level grids. By the $\mathscr{P}_1$ interpolation, as illustrated by Fig. 4, variables at each point in the fine level grid can be determined through the variables at the nodes of the parent cell in either coarse-level grid or fine-level grid.

For a fine-level node with coordinates (x, y) belonging to a parent cell defined by nodes (x_i, y_i) in the coarse-level or fine-level grids, the values at (x, y) is then approximated by

$$\xi(x,y) = \sum_{i=1}^{3} N_i(x,y)\xi(x_i, y_i), \qquad (18)$$

where $N_i(x,y)$ are the Lagrange basis polynomials.

The C2N projects variables from the coarse-level grid to the fine-level grid. First, the variables from the cell center are projected to the nodes of the coarse-level grid by using the natural neighbor interpolation. Then we use N2N to interpolate variables at each node of the fine-level grid.

Eq. (18) represents a discrete representation of the reconstruction operator $\mathscr{R}$ shown in Eqs. (15) and (16), i.e.,

$$\xi(x,y) = \widetilde{\mathscr{R}}\xi_j^{\text{cell-center}} \qquad (19)$$

where $\widetilde{\mathscr{R}}$ is the discrete reconstruction. By Eq. (19), the values at desired fine-level points are estimated through values at cells centers in the coarse-level grid.

4.4.2. Updating the coarse-level fracture path

In our model, the fracture path is represented directly in the computational grid. Hence, the information transfer on the fracture path from the fine-level model to the coarse-level model is dependent on the grid resolution on the two scales. Critical for simulation efficiency, small increases in the fracture length on the fine-level domain are not immediately projected to the coarse-level problem. Instead, for a fracture propagating on the fine level, with added length $|\Delta\omega_{ik}|$, the coarse-level fracture is updated only when $\left|\Delta\omega_{ik}^{\text{F}}\right| \geq \varepsilon_p \Delta H$, where ε_p is a simulation parameter. When this threshold is overcome, the coarse-level fracture is extended by a linear approximation of $\Delta\omega_{ik}^{\text{F}}$ and the coarse-level grid is updated as discussed in Section 4.1. Thus ε_p controls both the resolution of the coarse-level grid in the vicinity of propagating fractures and the numerical coupling strength between the fine-level and coarse-level models.

4.5. Numerical solution approach

As a summary of the above presentation, Fig. 5 illustrates the workflow of the two-level simulation approach. The time step size is usually taken as a constant represented by Δt. However, when a fracture propagates on the coarse level, both governing equations and parameters change along the fracture path, and the coarse-level state adjusts accordingly. In particular, the fractured part of the rock experiences

6

Table 1
Material properties.

Parameter	Definition	Value
E	Young's modulus	40 GPa
ν	Poisson's ratio	0.2
α	Biot's coefficient in the matrix	0.8
φ	Material porosity	0.01
c_p	Fluid compressibility	$4.0 \times 10^{-10} \, \text{Pa}^{-1}$
$\mathcal{K}$	Matrix permeability	$5.0 \times 10^{-20} \, \text{m}^2$
μ	Viscosity	$1.0 \times 10^{-4} \, \text{Pa} \bullet \text{s}$
μ_s	Friction coefficient	0.5
ψ	Dilation angle	1°
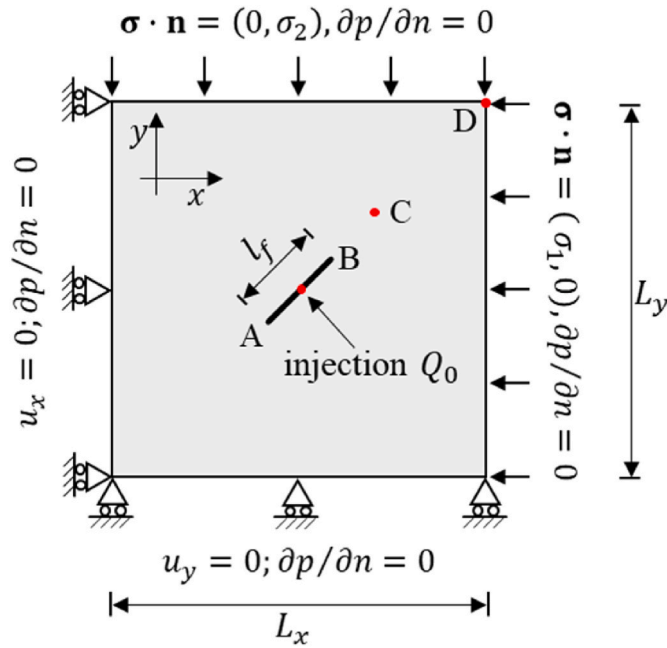
Fig. 6. Model of a porous media with a single fracture subjected to a principal stress regime.

enhanced permeability and volume available for fluids. The pressure field in the vicinity of the tip will adjust to the new parameters on a time scale that is much shorter than that of pressure diffusion related to the injection. We capture this effect by temporarily reducing the time step size with a factor $\varepsilon = 10^{-2}$ until this rapid dynamics is resolved and the pressure field near the crack tip is stabilized, whereupon we continue with the standard step size.

5. Results

The correctness of either the fine-level model or coarse-level model has been verified in previous studies.[5,17,19,33] This section, therefore, is devoted to the presentation of numerical experiments of the fully coupled model. The coarse-level problem alone may strain the available computational resources in application-oriented simulations with large domains and multiple fractures. Therefore, it is paramount to limit the additional computational cost to incorporate fracture propagation in such simulations. We have devised a suite of numerical experiments designed to investigate the stability, accuracy, and computational efficiency of the proposed numerical approach. Specifically, we study how the prediction of the fracture path is altered under variations in the size of the fine-level domain ($l = l_x = l_y$), the mesh size on the fine-level (Δh) and coarse-level (ΔH) domains, the time step size (Δt), and the threshold for updating the coarse-level geometry (ε_p). Together, these simulation parameters determine the balance between solution accuracy and computational cost. As our motivation is to allow simulations on large domains where high-resolution simulations are not feasible, our focus is not on the convergence of the numerical solution but rather its stability as the resolution in time and space are coarsened. Based on observations from these tests, we finally present a complex case of hydromechanical processes interacting with the deformation and propagation of multiple pre-existing fractures in a synthetic subsurface fluid injection scenario. The source code for the following simulations is open access.[64]

5.1. Onset of fracture

We first investigate how the onset of fracturing, determined by SIFs, is influenced by the size of the time step, coarse-level grid, and fine-level domain. To that end, we consider a porous media domain assumed to be homogenous and linearly elastic with the material properties given in Table 1. The geometry and boundary conditions of the model are
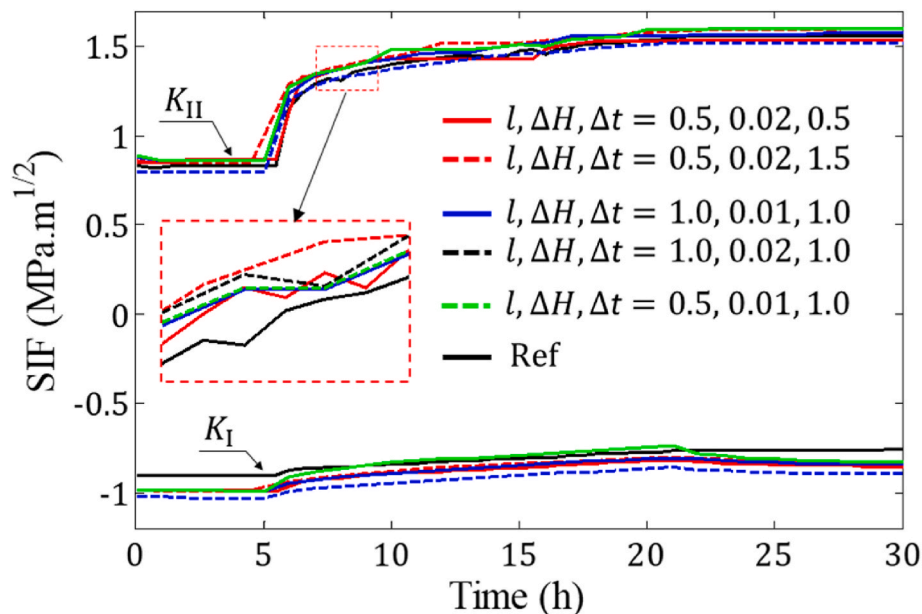

Fig. 7. Stress intensity factors at tip A obtained by different microdomain sizes l (m), mesh sizes ΔH (m), and time steps Δt (h).
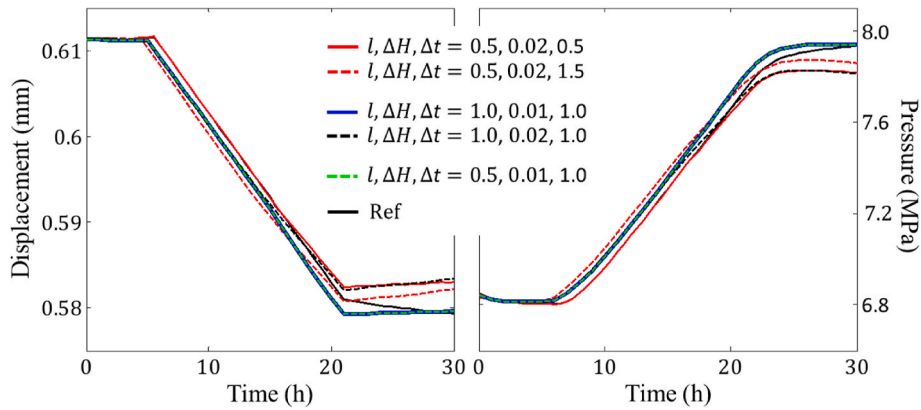
Fig. 8. Displacement at point D and pressure at point C obtained by different microdomain sizes l (m), mesh sizes ΔH (m), and time steps Δt (h).

illustrated in Fig. 6, in which $L_x = L_y = 2$ m. A single fracture of length $l_f = 0.1$ m and initial aperture $a^0 = 1$ mm is located at the center of the computational domain and oriented at 45° to the positive x-direction. The left and bottom boundaries are fixed in the x- and y-directions, respectively, and the top and right boundaries are free. The fluid is not allowed to flow through boundaries. The fractured porous media is subject to a stress state with the maximum horizontal stress $\sigma_1 = 20$ MPa and the minimum vertical stress $\sigma_2 = 10$ MPa, imposed orthogonally to the domain along the x- and y-directions, respectively. Water is injected into the pre-existing fracture after 6 h (h) and continuously for 15 h at a constant rate of $Q_0 = 5 \times 10^{-9} \text{m}^2/\text{s}$.

The effects of the time step (Δt), size of the fine-level domain (l), and mesh size (ΔH) on SIFs, displacement, and pressure are considered. Two levels of the fine-level domain size are considered, i.e., $l = 0.5$ m or 1.0 m. The resolutions of the fine-level and coarse-level domains are the same, i.e., $\varepsilon_m = 1.0$, and we consider two different levels: $\Delta H = \Delta h = 0.01$ m or 0.02 m. Three levels of time steps are used: $\Delta t = 0.5$ h, 1.0 h, or 1.5 h. Because of the lack of experimental data and exact solutions, the results from a computational setup are chosen as the reference. In the reference setup, the fine-level domain coincides with the coarse-level domain, i.e., $l = L$, and they are similar in resolution, i.e., $\Delta H = 0.01$ m, $\varepsilon_m = 1.0$. We also use a small-time step, i.e., $\Delta t = 0.5$ h, in this setup.

The SIFs at tip A, pressure at point C $= (1.5, 1.5)$, and displacement at point D $= (2, 2)$ obtained by different fine-level domain sizes, mesh sizes, and time steps are shown in Figs. 7 and 8. There are no significant differences in the solutions obtained by using a small fine-level domain compared to using a larger domain for a given mesh size ΔH. In addition, the resolution of meshes and time steps have little effect on the solution. These agreements indicate that the calculation of SIFs is stable for the considered time steps, fine-level domain sizes, and mesh sizes.

The injection at a low rate gradually builds up pressure, causing slip of the pre-existing fracture and shear failure instead of tensile failure at the fracture tip. As shown in Fig. 7, the injection increases K_{II} from 0.79 MPa • m$^{1/2}$ to 1.47 MPa • m$^{1/2}$, while there is almost no effect on K_I. This is the result of the gradual reduction of the contact traction at the pre-existing fracture during the injection. In addition, the injection also increases pore pressure and resists deformation of the domain caused by compression. As shown in Fig. 8, the pore pressure at point C and displacement at point D are 6.8 MPa and 0.63 mm, respectively, at the beginning of the injection. After 15 h of injection, pressure increases to 8.0 MPa and displacement decreases to 0.60 mm. Termination of injection keeps the pore pressure and displacement stable.

5.2. Wing-crack propagation caused by fluid injection

Next, we consider further aspects of the model and solution strategy by studying the initiation and propagation of wing cracks from the ends of a pre-existing fracture caused by gradual pressure build-up by fluid injection at a low rate. The problem geometry, boundary conditions, and material parameters are the same as in the previous example. The fracture toughness is $K_{IC} = 0.7$ MPa • m$^{1/2}$. Water is injected at a constant rate of $Q_0 = 5 \times 10^{-9} \text{m}^2/\text{s}$ into the pre-existing fracture during the simulation. The simulation is stopped when the wing crack propagating from tip A reaches a length of 0.25 m. To facilitate comparison between different sets of simulations, a reference case is computed with the same simulation parameters as used for the reference in Section 5.1, where we additionally use a threshold of $\varepsilon_p = 0.5$ for the coarse-level propagation of the fracture.

5.2.1. Simulation study of coupled physics

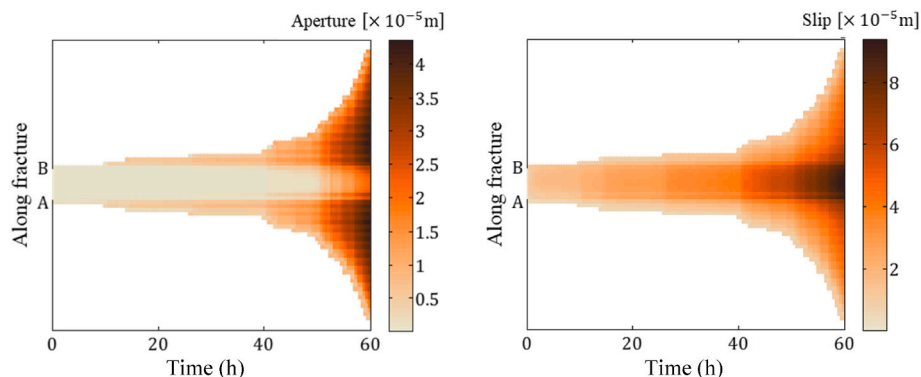We start by illustrating the capacity of the present model to capture

Fig. 9. Aperture expansion and shear slip at the fracture during simulation.
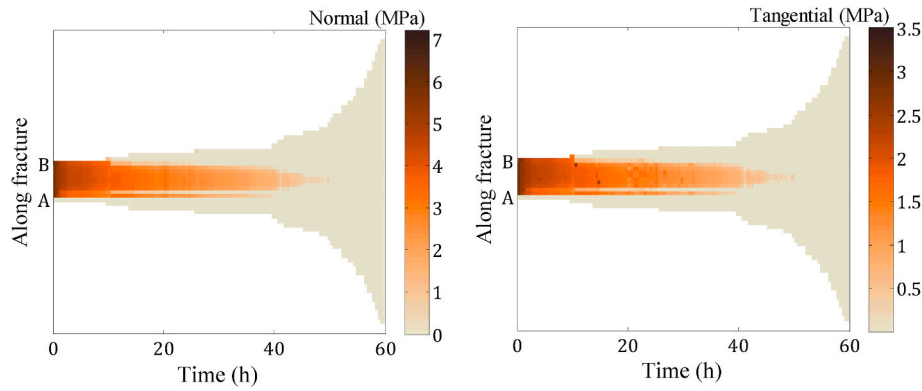
Fig. 10. Normal and tangential tractions at the fracture during simulation.
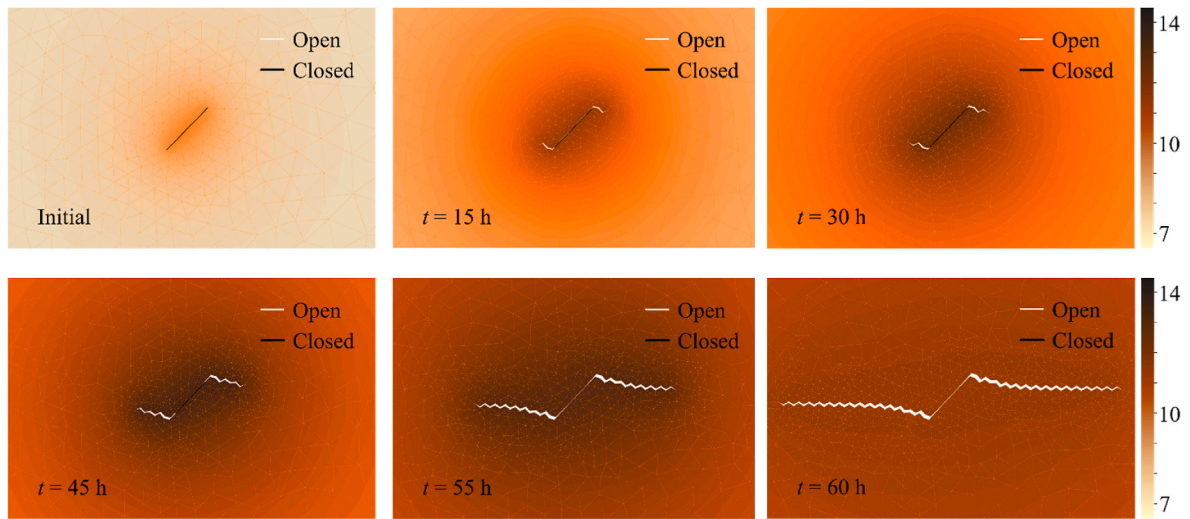

Fig. 11. Fracture propagation and pressure evolution in a 2D porous media during the fluid injection into the pre-existing fracture. Solid white/black lines denote fractures. The color bar represents pore pressure (MPa). (For interpretation of the references to color in this figure legend, the reader is referred to the Web version of this article.)

the complex coupled physics involved in fracture deformation and propagation based on a study of results from the reference case. Figs. 9 and 10 show the aperture expansion, shear slip, and contact traction of the fracture during the simulation. The fracture slowly extends in the first 40 h, but then it suddenly increases more quickly. Due to injection at a relatively low rate and low permeability of the matrix, pressure

takes time to build up in the porous media domain. This process gradually reduces the fracture contact traction and causes small slips on the fracture surface, but the fracture is still in contact. The small slip causes slight growth along the pre-existing fracture. After approximately 40 h of injection, the fluid pressure is sufficiently elevated in the domain to decrease the contact traction and induce slip in larger regions of the pre-
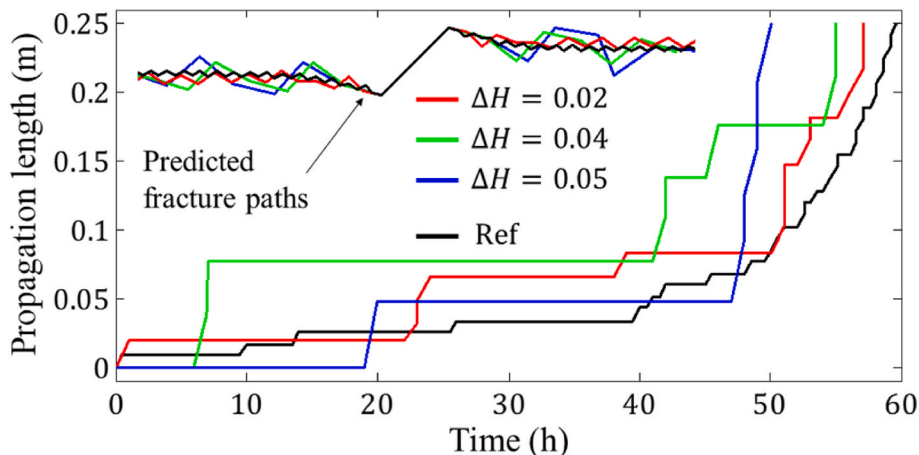

Fig. 12. The propagation length (m) from tip A and predicted fracture paths obtained by different resolutions ΔH (m) for $l = L$, $\varepsilon_p = 1.0$, and $\Delta t = 1.0$ h.
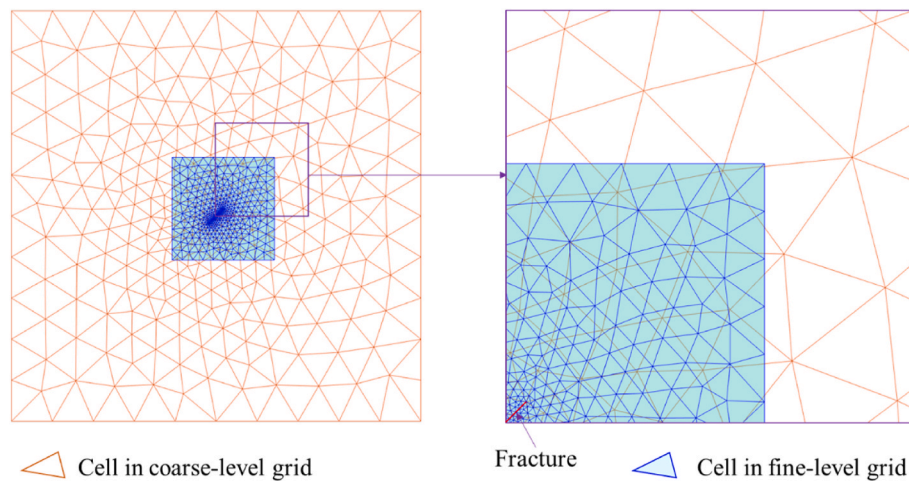
Fig. 13. The overlapping between coarse-level grid and fine-level grid for case $\Delta H = 0.02$, $l = 0.5$, and $\varepsilon_m = 0.25$.

existing fracture, leading to the further propagation of wing cracks. Finally, the contact traction goes to zero along the initial fracture, leading to its complete opening and rapid propagation.

The fracture geometry and surrounding pore pressure for the simulations are shown in Fig. 11. First, the slip of fracture faces triggers wing cracks to initiate from the tips. Then, fractures slowly propagate toward the maximum horizontal stress direction (the *x*-direction) during the first 40 h. High fluid pressure mainly occurs along the pre-existing fracture due to the low permeability of the surrounding porous medium. After that, the fracture extension makes fluid pressure propagate further in the domain while injection continues to elevate the pressure. This process reduces contact traction and causes the fracture to grow farther.

In the first 10 h, pressure and slip in the injected fracture increase gradually, but not enough to trigger the fracture to propagate. So, the coarse-level computational grid and solution are preserved. After that, wing cracks emerge and require the grid adjustment, followed by the update of the solution.

5.2.2. Effect of coarse-level grid resolution

To probe the robustness of the two-level simulation approach, we first investigate the effect of coarse-level grid resolution on predicting the speed of fracture growth and fracture paths. In this example, the fine-level grid coincides with the coarse-level grid, i.e., $l = L$, and $\varepsilon_m =$

1.0, while the time step is $\Delta t = 1.0$ h. A comparison of predictions obtained by different resolutions is shown in Fig. 12, in which black lines represent a prediction based on the computational reference.

For all grid resolutions, the wing cracks propagate in the direction normal to the least principal stress, although the fracture paths can be seen to meander, particularly for the coarser grids. The propagation speed is initially stable with small increments in fracture size, followed by accelerated propagation starting at 40–50 h for the different grid resolutions. The results are in relatively good agreement in the first period, although the timing of the propagation events varies between the grid resolutions. The results differ more in the acceleration period, with the coarsest resolution ($\Delta H = \Delta h = 0.05$ m) showing almost brutal fracturing compared with the gradual although accelerating speed for the solutions obtained on the more refined grids. This is not unexpected since fast propagation is hard to capture, particularly for coarse grid resolutions. The example thus illustrates the balance between accuracy and computational cost and underlines the need to adapt and refine the coarse-level grid in the vicinity of a propagating fracture tip.

5.2.3. Effect of fine-level domain size and grid resolution

Next, we consider the impact of seeking computational savings in the fine-level problem by assigning a smaller fine-level domain size l and different resolutions in the fine-level grids. We fix the time step to $\Delta t = 1.0$ h and set the resolution of the coarse-level domain and propagation
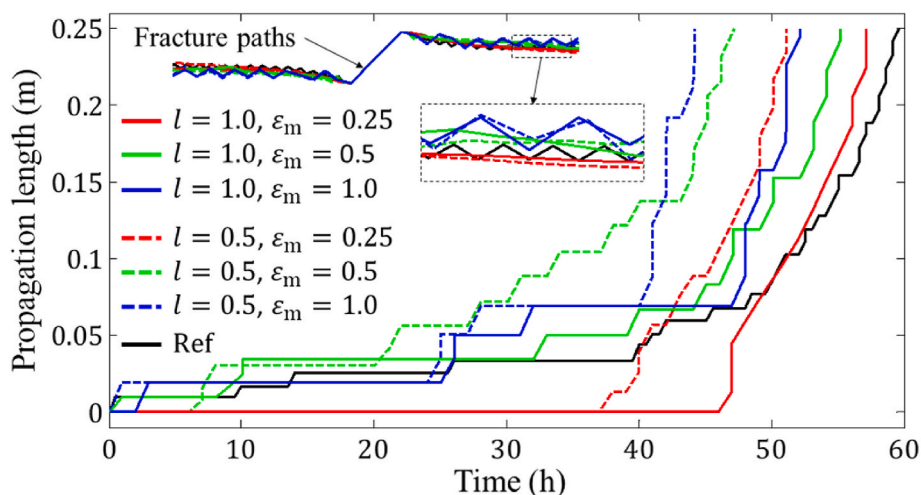

Fig. 14. The propagation length from tip A and fracture paths obtained by different sizes of the fine-level domain, l (m), and resolutions of the fine-level domain, ε_m, for $\Delta H = 0.02\,m$, $\Delta t = 1.0\,h$, and $\varepsilon_p = 0.5$.

a) Effect of time step Δt (h) for $l = 1.0$ m, $\Delta H = 0.01$ m, $\varepsilon_m = 1.0$, and $\varepsilon_p = 1.0$

b) Effect of propagation threshold ε_p for $l = 1.0$ m, $\Delta H = 0.02$ m, $\varepsilon_m = 1/3$, and $\Delta t = 1.0$ h
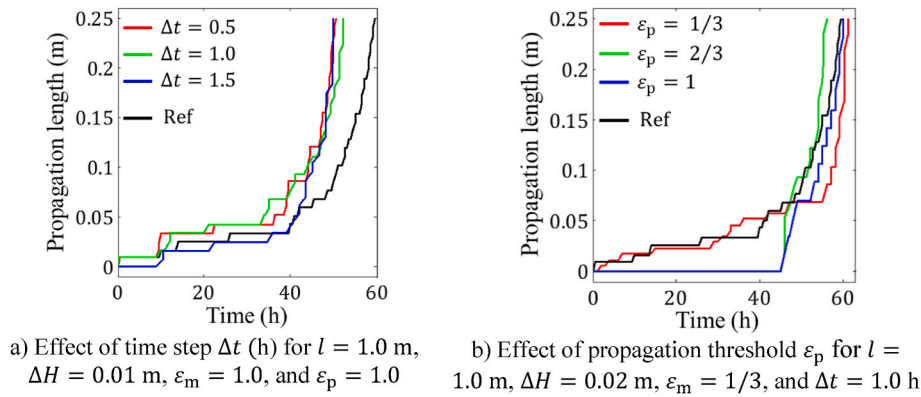
Fig. 15. The propagation length from tip A obtained by different resolutions, fine-level domain sizes, time steps, and propagation thresholds.

threshold to $\Delta H = 0.02$ m and $\varepsilon_p = 0.5$, respectively. The failure criterion is evaluated from a solution to the fine-level problem on a domain surrounding the fracture tip. The mesh for case $\Delta H = 0.02$, $l = 0.5$, and $\varepsilon_m = 0.25$ is shown in Fig. 13.

The effect of the fine-level domain size, l, and the resolution, $\Delta h = \varepsilon_m \Delta H$, of this fine-level domain on the propagation speed and fracture path is shown in Fig. 14. Again, the calculated fracture paths meander for the coarser grid, but this effect abates with the refinement of the fine-level grid. In terms of propagation speed, the simulations again show a transition from stable to accelerating propagation. Except for ε_m in the period from approximately 8 h–20 h after the start of the injection, the propagation speed is always larger for the smaller fine-level domains. As the boundary conditions for the fine-level problem are fixed by the coarse-level state, the smaller domains must absorb the energy from fracture sliding in a smaller rock volume, increasing the stresses in the vicinity of the tip. The severity of this effect should, to a large degree, be independent of the size of the coarse-level domain, and thus, using only somewhat larger fine-level domains should also be feasible for larger problems.

The impact of varying the fine-level mesh size is less clear. The results obtained on the two coarser fine-level grids, $\varepsilon_m = 0.5$ and $\varepsilon_m = 1.0$, are in broad agreement in the period of stable propagation but exhibit notable differences when transitioning to an accelerating regime. The results from the finest fine-level grid do not show a period of stable propagation on the coarse-level grid but instead enter the period of acceleration directly, at approximately the same time as the other simulations. This disagrees with the other results, notably the observation in Fig. 7 that the critical threshold for K_{II} is crossed approximately 7 h after the start of injection. A possible explanation is that the relatively large difference in mesh size between the fine-level and coarse-level problems for this value of ε_m makes the fracture propagate on the fine level without this effect being captured on the coarse-level domain.

5.2.4. Effect of discretization coupling parameters: time-step size and coarse-level propagation threshold

The effects of time step and threshold to extend fracture in the coarse-level domain are investigated in this example. For the time step study, as shown in Fig. 15 (a), we fix the size of the fine-level domain and mesh resolutions, i.e., $l = 1.0$ m and $\Delta H = \Delta h = 0.01$ m, and consider three levels of the time step, i.e., $\Delta t = 0.5$ h, 1.0 h, or 1.5 h. The method can be seen to be stable under this variation with a similar speed of fracture propagation in all three cases. The difference from the reference case can be attributed to the smaller size of the fine-level domain.

Besides, we also consider how the coarse-level propagation threshold, ε_p, affects the propagation speed, as shown in Fig. 15 (b). In this case, we set $l = 1.0$ m, $\Delta H = 0.02$ m, $\Delta t = 1.0$ h, and $\varepsilon_m = 1/3$ and assign three different values for ε_p, namely, $1/3$, $2/3$, or 1. For the two highest values of ε_p, i.e., $2/3$ and 1, there is no period of stable
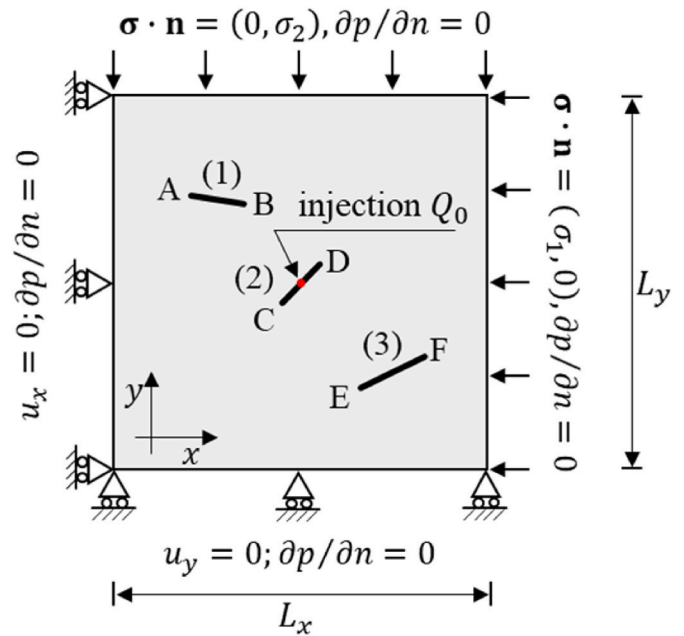

Fig. 16. Model of three fractures in a porous media subject to boundary conditions.

propagation on the coarse level but rather an abrupt transition to the accelerating regime. This is like the results reported in Fig. 14, which also had a small value of $\varepsilon_m = 1/4$. Using a small value for ε_p also compensates for this effect.

The findings of these experiments are summarized as follows. First, the direction of propagation is mainly controlled by boundary conditions. However, the computed fracture path tends to wiggle unless a relatively fine grid is applied on the fine-level domain. Such refined grids may again lead to delayed propagation on the coarse-level grid unless the fine-level and coarse-level problems are tightly coupled through the parameter ε_p. Second, the size of the fine-level domain can be reduced to lower the computational cost. However, a microdomain that is too small can overestimate the propagation speed. Finally, the time step size had little impact on the results for the cases we considered.

5.3. Extension: propagation of multiple fractures under fluid injection

Finally, to show the power of the proposed approach, hydromechanical processes interacting with the deformation and propagation of three pre-existing fractures in porous media are studied. The geometry and boundary conditions are illustrated in Fig. 16, in which $L_x = L_y =$
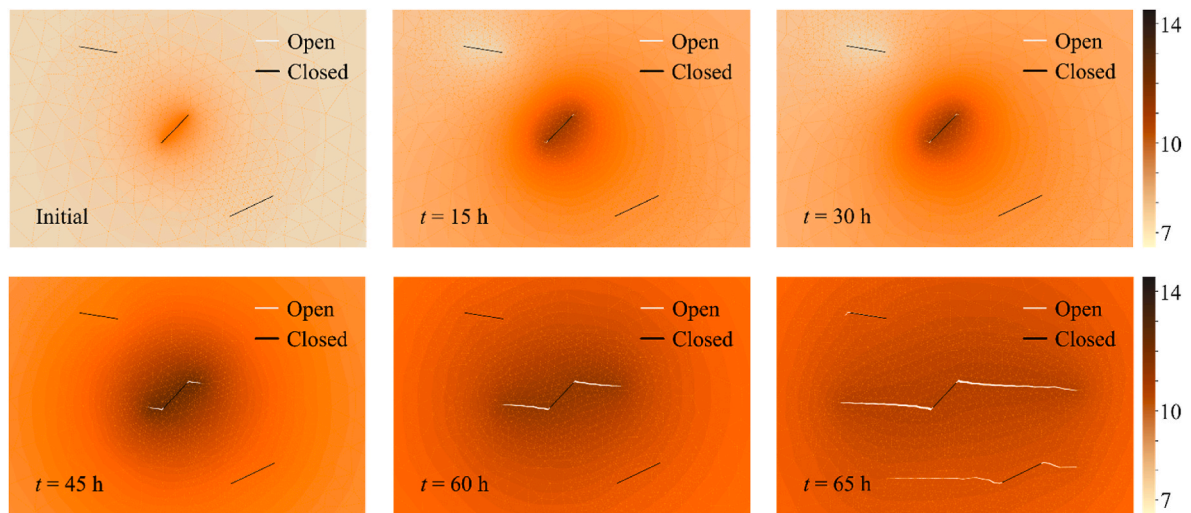
Fig. 17. Propagation of multiple fractures and evolution of pressure in a 2D porous media during fluid injection into one pre-existing fracture. Solid white/black lines denote fractures. The color bar represents pore pressure (MPa). (For interpretation of the references to color in this figure legend, the reader is referred to the Web version of this article.)

2 m. There are three fractures with the same initial aperture, $a_t^0 = 1$ mm, pre-existing in the domain. Fracture 1 is defined by endpoints A $=$ $(0.751, 1.208)$ and B $= (0.849, 1.192)$, fracture 2 by endpoints C $=$ $(0.965, 0.965)$ and D $= (1.035, 1.035)$, and fracture 3 by endpoints E $=$ $(1.144, 0.780)$ and F $= (1.256, 0.831)$. Water is injected at a constant rate of $Q_0 = 5 \times 10^{-9} \text{m}^2/\text{s}$ into fracture 2 during the simulation. The material parameters are the same as for the example in Section 5.2. The simulation is implemented based on the two-level model, in which $l =$ 0.5 m, $\Delta H = 0.02$ m, $\varepsilon_\text{m} = 0.5$, $\varepsilon_\text{p} = 0.5$, and $\Delta t = 1$ h.

The evaluation of the fracture geometry and the pore pressure is shown in Fig. 17. As in the above example, wing cracks mainly initiate and propagate from the fracture where fluid is injected. Small wing cracks are also observed from the other pre-existing fractures and are caused mainly by mechanical effects, i.e., the deformation of the domain. The fractures where fluid is injected propagate as a consequence of the hydromechanical stresses induced by the fluid injection, and fluid infiltrates farther into the domain as the fracture grows. These processes take place at the same time, leading the fracture to grow increasingly faster. In addition to the fracture growth, the injection also stimulates the nearby fracture to propagate.

6. Conclusion

This work presented a mathematical model and a numerical solution for coupling fluid flow, matrix deformation, fracture slip, and fracture propagation in porous media due to fluid injection. The governing mathematical model is based on Biot's model, with the deformation of existing fractures represented by contact mechanics. The maximum tangential stress criterion is combined with Paris' law to govern the fracture growth processes. A two-level simulation approach was presented, that employs a novel combination of finite volume methods for the poroelastic deformation of existing fractures with a finite element approach for the fracture propagation process.

The two-level approach allows for balancing between computational cost and simulation accuracy by varying the coupling between the coarse-level and fine-level models; tuning of the coupling strength should be done with respect to the problem to be solved, but also the computational resources available. The verifications in this paper show that the proposed approach is stable with different time steps, coarse-level grid sizes, and fine-level grid sizes. This approach is capable of simulating complex problems, such as the simultaneous propagation of multiple fractures combined with the slip and dilation of fractures in

contact and tensile opening. Hydraulically and mechanically interacting fractures are handled naturally. Therefore, the current model has potential in the simulation of mixed-mechanism hydraulic stimulation of fractured reservoirs, in which both fracture shearing and corresponding wing-crack propagation lead to an increase in permeability.

Declaration of competing interest

Data availability

The source code for this research can be found at: https://doi.org/10.5281/zenodo.5642548

Acknowledgments

References

1 Schoenball M, Ajo-Franklin JB, Blankenship D, et al. Creation of a mixed-mode fracture network at mesoscale through hydraulic fracturing and shear stimulation. *J Geophys Res Solid Earth.* 2020;125(12), e2020JB019807. https://doi.org/10.1029/2020JB019807.

2 McClure MW, Horne RN. An investigation of stimulation mechanisms in Enhanced Geothermal Systems. *Int J Rock Mech Min Sci.* 2014;72:242–260. https://doi.org/10.1016/j.ijrmms.2014.07.011.

3 Jung R. Egs — goodbye or back to the future. In: *Effective and Sustainable Hydraulic Fracturing.* InTech; 2013:95–121. https://doi.org/10.5772/56458.

4 Rutqvist J, Stephansson O. The role of hydromechanical coupling in fractured rock engineering. *Hydrogeol J.* 2003;11(1):7–40. https://doi.org/10.1007/S10040-002-0241-5.

5 Berre I, Stefansson I, Keilegavlen E. Fault slip in hydraulic stimulation of geothermal reservoirs: governing mechanisms and process-structure interaction. *Lead Edge.* 2020;39(12):893–900. https://doi.org/10.1190/tle39120893.1.

6 Pine RJ, Batchelor AS. Downward migration of shearing in jointed rock during hydraulic injections. *Int J Rock Mech Min Sci Geomech Abstracts.* 1984;21(5):249–263. https://doi.org/10.1016/0148-9062(84)92681-0.

7 Berre I, Doster F, Keilegavlen E. Flow in fractured porous media: a review of conceptual models and discretization approaches. *Transport Porous Media.* 2019;130(1):215–236. https://doi.org/10.1007/s11242-018-1171-6.

8 Salimzadeh S, Khalili N. A fully coupled XFEM model for flow and deformation in fractured porous media with explicit fracture flow. *Int J GeoMech*. 2015. https://doi.org/10.1061/(ASCE)GM.1943-5622.0000623. Published online December 1.

9 Khoei AR, Vahab M, Haghighat E, Moallemi S. A mesh-independent finite element formulation for modeling crack growth in saturated porous media based on an enriched-FEM technique. *Int J Fract*. 2014;188(1):79–108. https://doi.org/10.1007/s10704-014-9948-2.

10 Mohammadnejad T, Khoei AR. An extended finite element method for hydraulic fracture propagation in deformable porous media with the cohesive crack model. *Finite Elem Anal Des*. 2013;73(Supplement C):77–95. https://doi.org/10.1016/j.finel.2013.05.005.

11 Lecampion B. An extended finite element method for hydraulic fracture problems. *Commun Numer Methods Eng*. 2009;25(2):121–133. https://doi.org/10.1002/cnm.1111.

12 Shi F, Wang X, Liu C, he Liu, Wu H. An XFEM-based method with reduction technique for modeling hydraulic fracture propagation in formations containing frictional natural fractures. *Eng Fract Mech*. 2017;173. https://doi.org/10.1016/j.engfracmech.2017.01.025.

13 Khoei AR, Hirmand M, Vahab M, Bazargan M. An enriched FEM technique for modeling hydraulically driven cohesive fracture propagation in impermeable media with frictional natural faults: numerical and experimental investigations. *Int J Numer Methods Eng*. 2015;104(6):439–468. https://doi.org/10.1002/nme.4944.

14 Nordbotten JM, Boon WM, Fumagalli A, Keilegavlen E. Unified approach to discretization of flow in fractured porous media. *Comput Geosci*. 2019;23(2):225–237. https://doi.org/10.1007/s10596-018-9778-9.

15 Mikelić A, Wheeler M, Wick T. A phase-field method for propagating fluid-filled fractures coupled to a surrounding porous medium. *Multiscale Model Simul*. 2015;13(1):367–398. https://doi.org/10.1137/140967118.

16 Franceschini A, Castelletto N, White JA, Tchelepi HA. Algebraically stabilized Lagrange multiplier method for frictional contact mechanics with hydraulically active fractures. *Comput Methods Appl Mech Eng*. 2020;368, 113161. https://doi.org/10.1016/j.cma.2020.113161.

17 Dang-Trung H, Keilegavlen E, Berre I. Numerical modeling of wing crack propagation accounting for fracture contact mechanics. *Int J Solid Struct*. 2020;204–205:233–247. https://doi.org/10.1016/j.ijsolstr.2020.08.017.

18 Gallyamov E, Garipov T, Voskov D, van den Hoek P. Discrete fracture model for simulating waterflooding processes under fracturing conditions. *Int J Numer Anal Methods GeoMech*. 2018;42(13):1445–1470. https://doi.org/10.1002/nag.2797.

19 Stefansson I, Berre I, Keilegavlen E. A fully coupled numerical model of thermo-hydro-mechanical processes and fracture contact mechanics in porous media. *Comput Methods Appl Mech Eng*. 2021;386, 114122. https://doi.org/10.1016/j.cma.2021.114122.

20 Adachi J, Siebrits E, Peirce A, Desroches J. Computer simulation of hydraulic fractures. *Int J Rock Mech Min Sci*. 2007;44(5):739–757. https://doi.org/10.1016/j.ijrmms.2006.11.006.

21 Weng X, Kresse O, Cohen C, Wu R, Gu H. Modeling of hydraulic fracture network propagation in a naturally fractured formation. *All Days*. 2011;24. https://doi.org/10.2118/140253-MS. Published online January.

22 Miehe C, Mauthe S, Teichtmeister S. Minimization principles for the coupled problem of Darcy–Biot-type fluid transport in porous media linked to phase field modeling of fracture. *J Mech Phys Solid*. 2015;82:186–217. https://doi.org/10.1016/j.jmps.2015.04.006.

23 Detournay E. Mechanics of hydraulic fractures. *Annu Rev Fluid Mech*. 2016;48(1):311–339. https://doi.org/10.1146/annurev-fluid-010814-014736.

24 Salimzadeh S, Usui T, Paluszny A, Zimmerman RW. Finite element simulations of interactions between multiple hydraulic fractures in a poroelastic rock. *Int J Rock Mech Min Sci*. 2017;99:9–20. https://doi.org/10.1016/j.ijrmms.2017.09.001.

25 Settgast RR, Fu P, Walsh SDC, White JA, Annavarapu C, Ryerson FJ. A fully coupled method for massively parallel simulation of hydraulically driven fractures in 3-dimensions. *Int J Numer Anal Methods GeoMech*. 2017;41(5):627–653. https://doi.org/10.1002/nag.2557.

26 Santillán D, Juanes R, Cueto-Felgueroso L. Phase field model of hydraulic fracturing in poroelastic media: fracture propagation, arrest, and branching under fluid injection and extraction. *J Geophys Res Solid Earth*. 2018;123(3):2127–2155. https://doi.org/10.1002/2017JB014740.

27 Gao Y, Detournay E. Hydraulic fracture induced by water injection in weak rock. *J Fluid Mech*. 2021; 927:A19. https://doi.org/10.1017/jfm.2021.770.

28 Carrier B, Granet S. Numerical modeling of hydraulic fracture problem in permeable medium using cohesive zone model. *Eng Fract Mech*. 2012;79:312–328. https://doi.org/10.1016/j.engfracmech.2011.11.012.

29 Boone TJ, Ingraffea AR. A numerical procedure for simulation of hydraulically-driven fracture propagation in poroelastic media. *Int J Numer Anal Methods GeoMech*. 1990;14(1):27–47. https://doi.org/10.1002/nag.1610140103.

30 Detournay E. Propagation regimes of fluid-driven fractures in impermeable rocks. *Int J GeoMech*. 2004;4(1):35–45. https://doi.org/10.1061/(ASCE)1532-3641(2004)4:1(35).

31 Lecampion B, Bunger A, Zhang X. Numerical methods for hydraulic fracture propagation: a review of recent trends. *J Nat Gas Sci Eng*. 2017;49. https://doi.org/10.1016/j.jngse.2017.10.012.

32 Berre I, Stefansson I, Keilegavlen E. Fault slip in hydraulic stimulation of geothermal reservoirs: governing mechanisms and process-structure interaction. *arXiv: Geophysics*. 2020. https://doi.org/10.1190/tle39120893.1. Published online August 25.

33 Berge RL, Berre I, Keilegavlen E, Nordbotten JM, Wohlmuth B. Finite volume discretization for poroelastic media with fractures modeled by contact mechanics. *Int J Numer Methods Eng*. 2020;121(4):644–663. https://doi.org/10.1002/nme.6238.

34 McClure MW, Horne RN. Investigation of injection-induced seismicity using a coupled fluid flow and rate/state friction model. *Geophysics*. 2011;76(6): WC181–WC198. https://doi.org/10.1190/geo2011-0064.1.

35 Ghassemi A, Zhou X. A three-dimensional thermo-poroelastic model for fracture response to injection/extraction in enhanced geothermal systems. *Geothermics*. 2011; 40(1):39–49. https://doi.org/10.1016/j.geothermics.2010.12.001.

36 Baisch S, Vörös R, Rothert E, Stang H, Jung R, Schellschmidt R. A numerical model for fluid injection induced seismicity at Soultz-sous-Forêts. *Int J Rock Mech Min Sci*. 2010;47(3):405–413. https://doi.org/10.1016/j.ijrmms.2009.10.001.

37 Nguyen TS, Selvadurai APS. A model for coupled mechanical and hydraulic behaviour of a rock joint. *Int J Numer Anal Methods GeoMech*. 1998;22:29–48.

38 Stefansson I, Keilegavlen E, Halldórsdóttir S, Berre I. *Numerical Modelling of Convection-Driven Cooling, Deformation and Fracturing of Thermo-Poroelastic Media*. Transp Porous Media; 2021. https://doi.org/10.1007/s11242-021-01676-1. Published online December.

39 Yan C, Fan H, Huang D, Wang G. A 2D mixed fracture–pore seepage model and hydromechanical coupling for fractured porous media. *Acta Geotech*. 2021;16(10):3061–3086. https://doi.org/10.1007/s11440-021-01183-z.

40 Yan C, Jiao YY. A 2D fully coupled hydro-mechanical finite-discrete element model with real pore seepage for simulating the deformation and fracture of porous medium driven by fluid. *Comput Struct*. 2018;196:311–326. https://doi.org/10.1016/j.compstruc.2017.10.005.

41 Yan C, Jiao YY, Zheng H. A fully coupled three-dimensional hydro-mechanical finite discrete element approach with real porous seepage for simulating 3D hydraulic fracturing. *Comput Geotech*. 2018;96:73–89. https://doi.org/10.1016/j.compgeo.2017.10.008.

42 Erdogan F, Sih GC. On the crack extension in plates under plane loading and transverse shear. *J Basic Eng*. 1963;85(4):519–525. https://doi.org/10.1115/1.3656897.

43 Paris P, Erdogan F. A critical analysis of crack propagation laws. *J Fluid Eng*. 1963;85(4):528–533. https://doi.org/10.1115/1.3656900.

44 Haeri H, Shahriar K, Fatehi Marji M, Moarefvand P. Experimental and numerical study of crack propagation and coalescence in pre-cracked rock-like disks. *Int J Rock Mech Min Sci*. 2014;67:20–28. https://doi.org/10.1016/j.ijrmms.2014.01.008.

45 E W, Engquist B. The heterogeneous multi scale methods. *Commun Math Sci*. 2003;1:87–132.

46 Dhia H ben. Global-local approaches: the Arlequin framework. *Eur J Comput Mech*. 2006;15(1-3):67–80. https://doi.org/10.3166/remn.15.67-80.

47 Feyel F. A multilevel finite element method (FE2) to describe the response of highly non-linear structures using generalized continua. *Comput Methods Appl Mech Eng*. 2003;192:3233–3244. https://doi.org/10.1016/S0045-7825(03)00348-7.

48 Abdulle A, Weinan E, Engquist B, Vanden-Eijnden E. The heterogeneous multiscale method. *Acta Numer*. 2012;21:1–87. https://doi.org/10.1017/S0962492912000025.

49 Barsoum RS. Triangular quarter-point elements as elastic and perfectly-plastic crack tip elements. *Int J Numer Methods Eng*. 1977;11(1):85–98. https://doi.org/10.1002/nme.1620110109.

50 Keilegavlen E, Berge R, Fumagalli A, et al. PorePy: an open-source software for simulation of multiphysics processes in fractured porous media. *Comput Geosci*. 2021; 25(1):243–265. https://doi.org/10.1007/s10596-020-10002-5.

51 Martin V, Jaffré J, Roberts J. Modeling fractures and barriers as interfaces for flow in porous media. *SIAM J Sci Comput*. 2005;26:1667–1691. https://doi.org/10.1137/S1064827503429363.

52 Zimmerman RW, Bodvarsson GS. Hydraulic conductivity of rock fractures. *Transport Porous Media*. 1996;23(1):1–30. https://doi.org/10.1007/BF00145263.

53 Anderson TL. *Fracture Mechanics: Fundamentals and Applications*. fourth ed. CRC Press; 2017.

54 Kim J, Moridis GJ. Development of the T+M coupled flow–geomechanical simulator to describe fracture propagation and coupled flow–thermal–geomechanical processes in tight/shale gas systems. *Comput Geosci*. 2013;60:184–198. https://doi.org/10.1016/j.cageo.2013.04.023.

55 Paluszny A, Matthäi SK. Numerical modeling of discrete multi-crack growth applied to pattern formation in geological brittle media. *Int J Solid Struct*. 2009;46(18):3383–3397. https://doi.org/10.1016/j.ijsolstr.2009.05.007.

56 Paluszny A, Zimmerman RW. Numerical simulation of multiple 3D fracture propagation using arbitrary meshes. *Comput Methods Appl Mech Eng*. 2011;200(9):953–966. https://doi.org/10.1016/j.cma.2010.11.013.

57 Geuzaine C, Remacle JF. Gmsh: a 3-D finite element mesh generator with built-in pre- and post-processing facilities. *Int J Numer Methods Eng*. 2009;79(11):1309–1331. https://doi.org/10.1002/nme.2579.

58 Keilegavlen E, Duboeuf L, Dichiarante AM, et al. Hydro-mechanical simulation and analysis of induced seismicity for a hydraulic stimulation test at the Reykjanes geothermal field, Iceland. *Geothermics*. 2021;97, 102223. https://doi.org/10.1016/j.geothermics.2021.102223.

59 Hüeber S, Wohlmuth B. A primal–dual active set strategy for non-linear multibody contact problems. *Comput Methods Appl Mech Eng*. 2005;194:3147–3166. https://doi.org/10.1016/j.cma.2004.08.006.

60 Nordbotten JM. Stable cell-centered finite volume discretization for Biot equations. *SIAM J Numer Anal*. 2016;54(2):942–968. https://doi.org/10.1137/15M1014280.

61 Nordbotten JM, Keilegavlen E. An introduction to multi-point flux (MPFA) and stress (MPSA) finite volume methods for thermo-poroelasticity BT - polyhedral methods in

geosciences. In: Formaggia L, Masson R, eds. *di Pietro DA*. Springer International Publishing; 2021:119–158. https://doi.org/10.1007/978-3-030-69363-3_4.

62 Parks DM. A stiffness derivative finite element technique for determination of crack tip stress intensity factors. *Int J Fract*. 1974;10(4):487–502. https://doi.org/10.1007/BF00155252.

63 Zienkiewicz OC, Zhu JZ. The superconvergent patch recovery and a posteriori error estimates. Part 1: the recovery technique. *Int J Numer Methods Eng*. 1992;33(7): 1331–1364. https://doi.org/10.1002/nme.1620330702.

64 Dang-Trung H. Simulation of injection induced fracture mechanics with runscripts. https://doi.org/10.5281/zenodo.5642548.